nature energy

Article

https://doi.org/10.1038/s41560-023-01387-5

Fast-charging capability of graphite-based lithium-ion batteries enabled by Li_3P-based crystalline solid–electrolyte interphase

Received: 10 December 2022

Accepted: 19 September 2023

Published online: 30 October 2023

Check for updates

Shuibin Tu[1,2,4], Bao Zhang[1,4], Yan Zhang[1], Zihe Chen[1], Xiancheng Wang[1], Renming Zhan[1], Yangtao Ou[1], Wenyu Wang[1], Xuerui Liu[1], Xiangrui Duan[1], Li Wang[3] & Yongming Sun[1]

Li^+ desolvation in electrolytes and diffusion at the solid–electrolyte interphase (SEI) are two determining steps that restrict the fast charging of graphite-based lithium-ion batteries. Here we show that the low-solvent-coordination Li^+ solvation structure could be induced near the inner Helmholtz plane on inorganic species. Specifically, Li_3P could enable a lower Li^+ desolvation barrier and faster Li^+ diffusion capability through the SEI in comparison to the regular SEI components. We construct an ultrathin S-bridged phosphorus layer on a graphite surface, which in situ converts to crystalline Li_3P-based SEI with high ionic conductivity. Our pouch cells with such a graphite anode show 10 min and 6 min (6C and 10C) charging for 91.2% and 80% of the capacity, respectively, as well as 82.9% capacity retention for over 2,000 cycles at a 6C charging rate. Our work reveals the importance of the SEI component and structure regulation for fast-charging LIBs.

Building fast-charging lithium-ion batteries (LIBs) is highly desirable to meet the ever-growing demands for portable electronics and electric vehicles[1–5]. The United States Advanced Battery Consortium set a goal for fast-charging LIBs, which requires the realization of >80% state of charge within 15 min (4C), as well as high energy density (>80% of full charge state or no less than 200 W h kg^{-1}), long lifespan and safety[6,7]. Until now, it has remained a challenge to achieve this goal even for state-of-the-art LIBs[1,8–10]. The graphite anode is widely regarded as the limiting component for the fast charging of a battery[11,12]. On the one hand, fast charging is limited by slow electrochemical reaction processes at the graphite surface, including Li^+ desolvation at the solid–electrolyte interphase (SEI) and Li^+ transport within the SEI[13–15]. On the other hand, graphite has a low overpotential tolerance due to its low equilibrium potential (~0.1 V versus Li/Li^+), which means that metallic Li is easily produced once the anode potential falls below 0 V (versus Li/Li^+) during charging, leading to inferior cycling stability and even safety concerns[16–18]. The above concerns are exacerbated for high-areal-capacity anodes, as the Li^+ transport kinetics are more sluggish.

In recent years, enormous endeavours have been dedicated to the realization of battery fast charging, among which SEI engineering demonstrates great promise[16,18–20]. An ideal SEI for fast-charging anodes should have a high Li^+ conductivity and be thin, which supports fast Li^+ transport at the electrode surface[21,22]. Furthermore, good electronic insulation and a compact structure can prevent continuous electrolyte reduction at the anode surface, as well as solvent intrusion into the SEI and its further intercalation into bulk graphite[21]. Inorganic Li^+-containing species have been widely accepted as good components (for example, LiF, Li_2CO_3, Li_2O, etc.) due to their good electronic insulation and overall acceptable ionic conductivity[16,23–25]. Till now, introducing these species in SEI by using electrolyte additives or highly concentrated electrolytes has been regarded as a successful strategy[26,27]. The Li^+ desolvation process at the electrode–electrolyte interphase plays a vital role in the fast-charging capability of the anode[14,18,28]. Using weakly solvating electrolytes could effectively improve the fast-charging performance of a graphite anode through reducing the activation energy of Li^+ desolvation[29]. Nevertheless, the

[1]Wuhan National Laboratory for Optoelectronics, Huazhong University of Science and Technology, Wuhan, China. [2]Department of Materials Science and Engineering, Huazhong University of Science and Technology, Wuhan, China. [3]Institute of Nuclear & New Energy Technology, Tsinghua University, Beijing, China. [4]These authors contributed equally to this work: Shuibin Tu, Bao Zhang. e-mail: yongmingsun@hust.edu.cn

fast-charging performance of graphite anodes is still far below expectations, especially for those with reasonably high mass loading. Moreover, a fundamental understanding and rational design of the SEI are still lacking for fast charging.

In this work, we demonstrate the important role of the SEI component in the Li^+ desolvation for fast charging in addition to its ionic conductivity and thickness. We found that SEI species with higher Li^+ adsorption energy could enable a faster desolvation process. Specifically, we consider Li_3P to be a promising SEI component due to its high ionic conductivity[30]. The effects of regular SEI components (organic components, Li_2O, Li_2CO_3 and LiF) and Li_3P on the Li^+ solvation structure at the interphase were investigated by combining molecular dynamics (MD) simulations and density functional theory (DFT). It was found that Li_3P has the strongest Li^+ affinity energy among the investigated components. According to the MD results, a solvation sheath with a low solvent coordination number can form near the inner Helmholtz plane (IHP) on the Li_3P interphase, supporting fast Li^+ desolvation. Blue graphite, with a ~4.4-nm-thick uniform S-bridged P layer firmly bonded on its surface (denoted P-S-graphite) was explored. A continuously crystalline Li_3P-based SEI was produced in situ during initial battery cycling. We demonstrated that the pouch cells, which consisted of $LiNi_{0.6}Co_{0.2}Mn_{0.2}O_2$ (NCM622), and the as-fabricated P-S-graphite, which had a reasonably high areal capacity of ~2.3 mAh cm^{-2}, showed excellent fast-charging performance (10 and 6 min charging time for 91.2% and 80% of the capacity, respectively) and stable cycling at a 6C charging rate (~1 Ah, 2,000 cycles and capacity retention rate of 82.9%). We emphasize the vital importance of the SEI component and structure in regulating the Li^+ solvation structure at the anode interphase and accelerating Li^+ desolvation for fast-charging LIBs. This work offers alternative avenues for SEI engineering for advanced LIBs considering stability and ionic conductivity.

Theoretical simulations

Desolvation of the solvated Li^+ at the anode interphase and Li^+ diffusion through the SEI are two factors that restrict the charging kinetics of anodes, which are highly related to the SEI components[31]. Herein, MD simulations were employed to understand the effect of Li_3P, the typical superionic Li^+ conductor, on the Li^+ solvation structure at the anode interphase and to compare Li_3P with regular SEI components, including organic (lithium ethylene mono-carbonate, LEMC) and inorganic components (Li_2O, Li_2CO_3 and LiF) (Fig. 1a–e and Supplementary Fig. 1). The solvation structure of the Li^+ near the IHP was counted from the calculated radial distribution functions (Supplementary Fig. 2). The dominant peaks of $g(r)$ appeared at 1.8 and 1.6 Å for Li^+–O (ethylene carbonate (EC)/dimethyl carbonate (DMC)) and Li–F(PF_6^-) pairs, respectively, and the coordination number of EC was much higher than that of DMC and PF_6^- in all SEI components. On the organic LEMC surface, Li^+ was almost completely solvated by approximately 3.51 EC molecules and 0.49 DMC molecules, with no PF_6^- involved in the solvation sheath. In contrast, the Li^+ solvation structures were quite different from the inorganic SEI components. Among these systems, Li^+ was partially desolvated on the Li_3P surface having the lowest coordination number of 2.63. Low coordination numbers of 3.33, 3.09 and 3.69 were also found for the Li_2CO_3, Li_2O and LiF surfaces, respectively. PF_6^- could penetrate the Li^+ solvation sheaths of Li_2CO_3, Li_2O and Li_3P with coordination numbers of 0.67, 0.82 and 0.33, respectively (Fig. 1f). A low-solvent-coordination Li^+ was more easily desolvated before diffusion through the SEI. In addition, DFT calculations were also performed to reveal the Li^+ adsorption behaviour of these different components (Supplementary Fig. 3). Li_3P displayed the strongest affinity energy for Li^+, whereas LEMC had the weakest affinity energy for Li^+ (Fig. 1g), which led to distinctly different Li^+ solvation structures near the IHP on the anode interphase and supported facile Li^+ desolvation on Li_3P. Metadynamics simulations were further performed to evaluate the potential of the mean force, which provided a free energy profile during the desolvation process. As shown in Supplementary Fig. 4, the potential of the mean force continued to increase as the Li^+ came close to the SEI surface, which was accompanied by a decrease in its coordination number. The desolvation barriers of the most common SEI components, LEMC and Li_2CO_3, were approximately 67.9 and 65.0 kJ mol^{-1}, respectively. This result was consistent with previous DFT-based tight-binding calculations of Li_2CO_3 (47–76 kJ mol^{-1}, depending on the surface charge)[32]. Benefiting from the strong Li^+ adsorption, the desolvation barrier on LiF decreased to 58.9 kJ mol^{-1}. Notably, the desolvation barriers on Li_2O and Li_3P significantly decreased to 55.0 and 50.5 kJ mol^{-1}, respectively. The above results again support that the inorganic SEI components were beneficial for accelerating the Li^+ desolvation process, especially for Li_3P. Together with the advantage of high ionic conductivity (Supplementary Table 1), Li_3P can be an ideal SEI component for the anode to achieve fast battery charging since it can accelerate Li^+ desolvation and diffusion through the SEI (Fig. 1h,i). Considering the importance of both the structure and components of the SEI, a compact Li_3P-based SEI is highly desirable for fast-charging batteries, which remains unexplored.

Design of Li_3P-based SEI on the graphite anode

Li_3P-based SEI can be produced on the anode surface through an irreversible electrochemical conversion of P to Li_3P during the battery formation cycle, as occurs for common inorganic species, such as Li_2O, Li_2CO_3 and LiF. However, the formation of a stable and uniform P interphase on the anode remains a significant challenge (Supplementary Fig. 5). In this work, we constructed an ultrathin P nanolayer on the graphite surface using the S molecule linking effect (P-S-graphite). We conducted MD simulations to theoretically explore the effect of S on the deposition behaviour of P using the classical vaporization–condensation approach for the fabrication of P-based composites[30]. The simulated process started with the rapid evaporation of samples at high temperatures, followed by rapid cooling to achieve the deposition of samples (Fig. 2a–c). In contrast to pure P, pure S could easily be deposited onto the surface of amorphous carbon due to the strong chemical bonding between C and S (Fig. 2a,b). Therefore, the S-bridged P interphase could be achieved on the carbon surface due to the formation of strong C–S and S–P bonds (Fig. 2c).

Experimentally, the red P/S hybrid and micrometre-sized graphite (Supplementary Fig. 6, 10–20 μm) were sealed and annealed for the vaporization–condensation process (Supplementary Fig. 7). During the initial heating process, cyclic S (S_8) molecules decomposed into chain-like S molecules above the melting point, which could be absorbed/confined by the amorphous carbon layer on the graphite surface in the form of short-chain S (S_2–S_4)[33]. When the temperature further increased to 416 °C, red P chains began to transform into P_4 molecules and interacted with S species on the graphite surface due to their strong affinity (Fig. 2d and Supplementary Fig. 8), resulting in the formation of a uniform P interphase on the graphite. Note that the uniform P could not be produced on the graphite surface without S (denoted as P-graphite) (Supplementary Fig. 9a).

Scanning electron microscopy (SEM) images show the coarse surface of P-graphite in contrast to the smooth surface structure of the pristine graphite and P-S-graphite (Supplementary Fig. 9b and Fig. 2e), indicating the significant role of S in homogenizing the P distribution on the graphite, which is consistent with the MD results. With an optimized S content of 1 wt% in the S/P hybrid (Supplementary Figs. 9 and 10), the initial grey of the pristine graphite turned blue for the P-S-graphite (Supplementary Fig. 11 and Fig. 2f). A uniform, compact and ultrathin P nanolayer (~4.4 nm) with an amorphous structure was observed on the P-S-graphite (~1.4 wt% P loading) by high-resolution transmission electron microscopy (HRTEM) (Fig. 2g). In addition to the HRTEM analysis, the amorphous structure of the P nanolayer was also verified by X-ray diffraction (Supplementary Fig. 12). The scanning transmission electron microscopy and the corresponding

https://doi.org/10.1038/s41560-023-01387-5

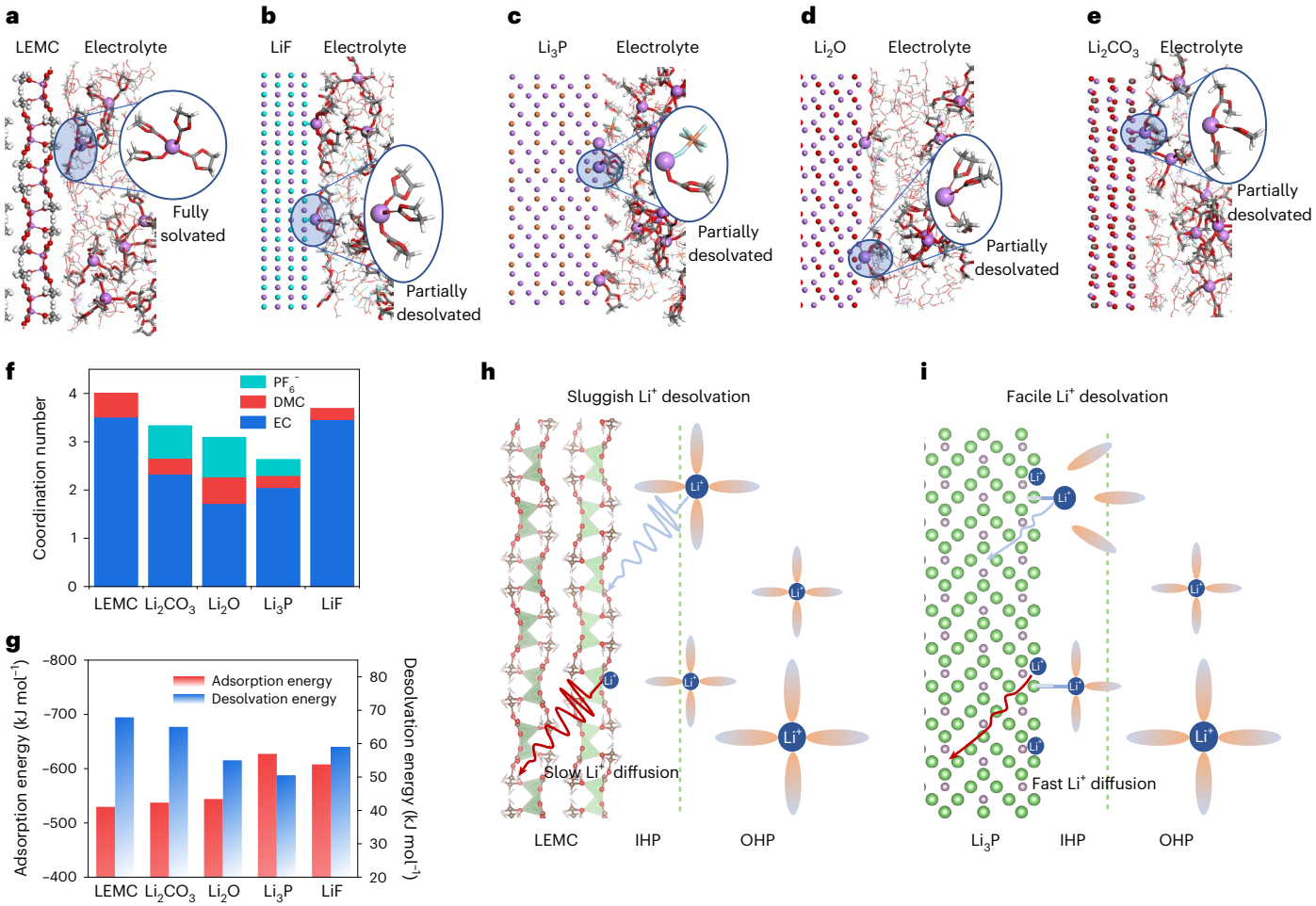

Fig. 1 | Theoretical studies of Li^+ solvation structure at the anode interphase. **a**–**e**, MD simulation snapshots of LEMC (**a**), LiF (**b**), Li_3P (**c**), Li_2O (**d**) and Li_2CO_3 (**e**) in 1 M $LiPF_6$ in EC/DMC at 298 K. Li^+ ions and coordinated molecules are depicted by large ball models and ball-and-sticks model, respectively. The wireframes represent the free solvents and PF_6^-. The simulation boxes are shown in Supplementary Fig. 1. The blue ellipses present the typical Li^+ solvation structures near the IHP. Atomic colour representation: violet for Li, cyan for F, red for O, grey for C and brown for P. **f**, Coordination number of the solvation structure near the IHP on various SEI species based on the MD simulation results. **g**, The affinity energy and desolvation barrier of various SEI components for Li^+. **h**, Schematic of the desolvation process and Li^+ transport within the LEMC-based SEI. The fully solvated Li^+ undergoes sluggish desolvation kinetics. The low ionic conductivity of LEMC results in slow Li^+ diffusion through the SEI. Li^+ ions and solvent-coordinated molecules are depicted by blue circles and orange ovals, respectively. LEMC is depicted by a polyhedral model. **i**, Schematic of the desolvation process and Li^+ transport within the Li_3P-based SEI. The partially desolvated Li^+ accelerates the desolvation kinetics. The high ionic conductivity of Li_3P enables fast Li^+ migration through the SEI. Li_3P is depicted by a ball model. OHP, outer Helmholtz plane.

elemental mapping images of P-S-graphite (Fig. 2h) also confirm the homogeneous distribution of P and S on the surface.

Figure 2i shows Raman spectra of P-S-graphite, P-graphite and pristine graphite. Except for the characteristic peaks of P ranging from 250 to 500 cm^{-1}, two new peaks at 165.9 and 205.5 cm^{-1} appeared for the P-S-graphite, which originated from the formation of P–S bonds[34]. The surface chemical state of P-S-graphite was further analysed by X-ray photoelectron spectroscopy (XPS). The typical characteristics of the S–P bond were detected at ~162.1 eV in the high-resolution S 2*p* XPS spectrum of P-S-graphite[34]. The peaks at ~163.3 and 164.5 eV were assigned to the C–S–C bond, and the peak at ~169.4 eV originated from the C–SO_n–C bond[35]. In addition, the C–S–P and P–S bonds were also verified in high-resolution C 1*s* and P 2*p* XPS spectra (Supplementary Fig. 13), which could enable the good air stability of P (Supplementary Fig. 14).

The initial charging/discharging curves of graphite anodes in half-cells are shown in Supplementary Fig. 15. A slightly extended potential slope at ~0.7 V was observed for the P-S-graphite (Supplementary Fig. 16) during the initial lithiation process in comparison to the pristine graphite anode, which could be ascribed to the conversion of P into Li_3P during the formation cycle[30]. The initial Coulombic efficiency of P-S-graphite was ~88.7% with a cutoff potential of 1.0 V (versus Li/Li^+) and close to that of pristine graphite (~90.5%), which indicated that the introduction of P on the graphite caused only a small amount of Li to be consumed.

An amorphous interphase layer with a thickness of ~18 nm was observed on the pristine graphite after ten repeated charge/discharge cycles according to the HRTEM investigation (Fig. 3a), which was in agreement with the structure and thickness of the SEI on graphite in previous reports[18]. Interestingly, a much thinner interphase layer (~8 nm) was observed on the P-S-graphite surface in comparison to the pristine graphite (Fig. 3b). A continuously crystalline layer with a *d*-spacing of 0.20 nm was observed by HRTEM (Fig. 3b–d) and its corresponding spotty fast Fourier transform analysis (Supplementary Fig. 17), which corresponded to the (103) crystal plane of Li_3P and supported the formation of a crystalline Li_3P-based SEI. The overall thickness of the SEI on the P-S-graphite was ~8 nm, which was much thinner than the ~18 nm for the pristine graphite and indicated the reduced Li^+ diffusion distance within the SEI.

https://doi.org/10.1038/s41560-023-01387-5

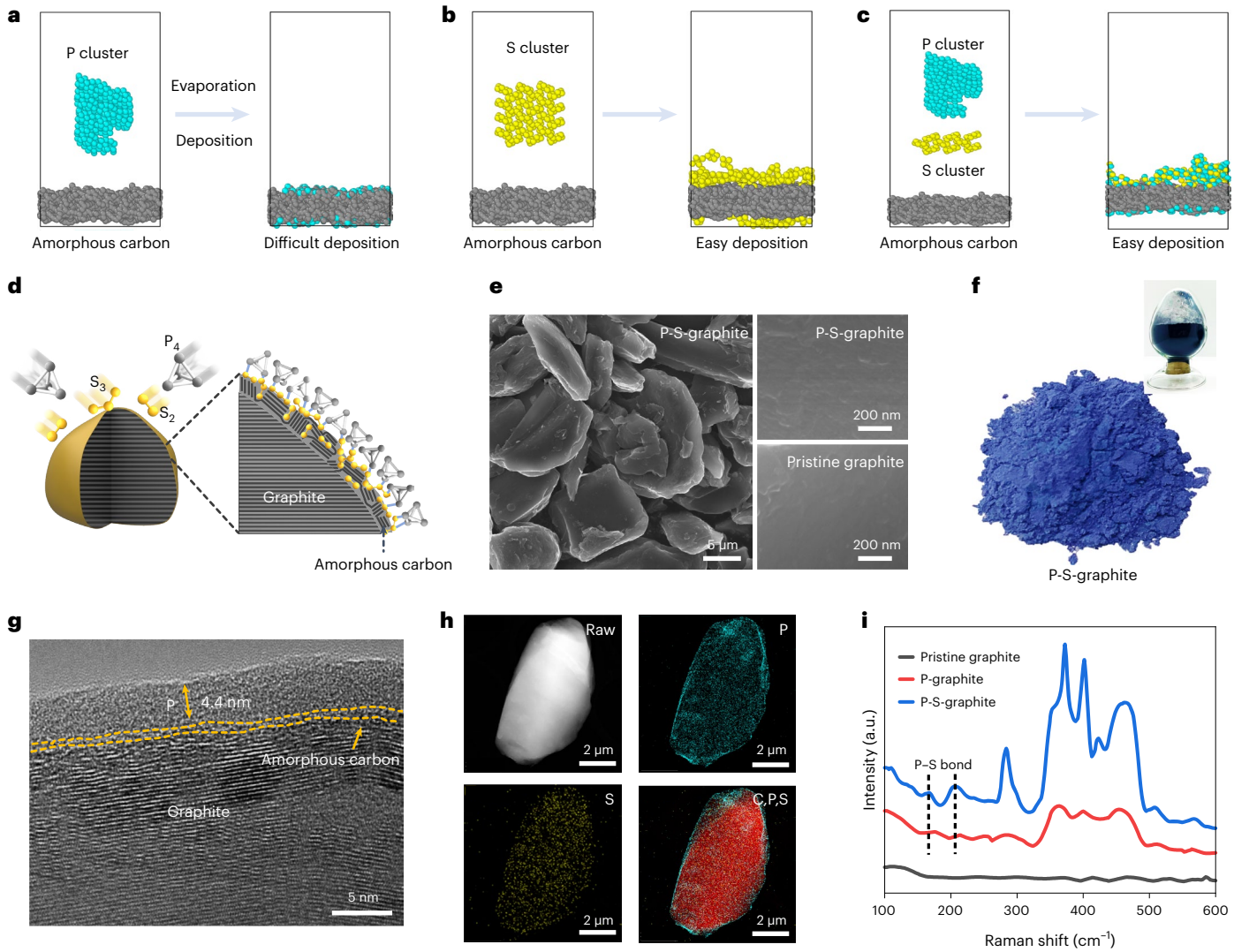

Fig. 2 | Fabrication of P-S-graphite. a–**c**, MD simulations of the deposition behaviour of pure P (**a**), pure S (**b**) and an S/P hybrid (**c**) on amorphous carbon. **d**, Schematic of the formation mechanism of P-S-graphite. S can facilitate uniform P deposition on graphite. **e**, SEM images of pristine graphite and P-S-graphite. **f**–**h**, Optical photographs (**f**), HRTEM (**g**) and elemental mapping images (**h**) of P-S-graphite. **i**, Raman spectra of P-S-graphite, P-graphite and pristine graphite.

An XPS analysis studied the chemical compositions and the states of the SEI. The high-resolution P 2*p* XPS spectrum of P-S-graphite showed three prominent peaks. The two peaks at 129.0 and 133.3 eV could be ascribed to Li_3P (ref. 36), and the other peak at 136.1 eV originated from the formation of P–F bonds[37] (Supplementary Fig. 18). The results from the high-resolution C 1*s* XPS spectra showed that the contents of organic species (C–O and C=O) in the P-S-graphite were much lower than those in the pristine graphite (Fig. 3e).

To investigate the interfacial resistance of the as-formed SEI on the P-S-graphite anode, temperature-dependent electrochemical impedance spectroscopy (EIS) was measured from 10 to 35 °C (Supplementary Fig. 19). Typically, the SEI resistance (R_{SEI}) and charge transfer resistance (R_{ct}) of P-S-graphite were, respectively, 2.3 and 20.3 Ω at room temperature (25 °C), much lower than those of pristine graphite (40.1 Ω for R_{SEI} and 43.1 Ω for R_{ct}). The one order of magnitude lower R_{SEI} of P-S-graphite than that of the pristine graphite could be attributed to the high Li^+ conductivity of Li_3P, and supported the fast Li^+ diffusion within the SEI. The significantly reduced R_{ct} could enable fast Li^+ transport at the interphase of P-S-graphite in comparison to pristine graphite. By fitting the EIS curves to the equivalent circuit model established at different frequencies (Supplementary Fig. 20), the values of the activation energy during Li^+ desolvation and its migration across the SEI were calculated according to the classic Arrhenius law. The Li^+ desolvation energy barrier ($E_{a,ct}$) of P-S-graphite (~46.9 kJ mol^{-1}) was much lower than that of pristine graphite (~58.0 kJ mol^{-1}) (Fig. 3f). The reduced desolvation activation energy was attributed to the high affinity of Li_3P for Li^+ and the low-solvent-coordination solvation structure near the IHP on the Li_3P interphase according to the DFT and MD results (Fig. 1). Additionally, a much lower activation energy for Li^+ diffusion through the SEI ($E_{a,SEI}$) was achieved for the P-S-graphite, which had a continuously crystalline Li_3P-based SEI in comparison to the pristine graphite, which had an organic-rich SEI (~25.8 versus ~52.7 kJ mol^{-1}) (Fig. 3g), supporting fast Li^+ transport capability at the P-S-graphite surface. Low-content S doping could slightly reduce the Li^+ desolvation barrier on the Li_3P surface according to the MD simulation results (Supplementary Fig. 21). Moreover, $E_{a,ct}$ and $E_{a,SEI}$ of the P-S-graphite anode, which had a continuously crystalline Li_3P-based SEI, were also lower than those of the graphite anode with a LiF-rich SEI or P-graphite anode (Supplementary Figs. 22 and 23).

The schematics in Fig. 3h,i depict the interphase structures of the pristine graphite and the P-S-graphite. A regular SEI of the pristine graphite could cause sluggish Li^+ desolvation and slow Li^+ transport within it (Fig. 3h). In contrast, the continuously crystalline Li_3P-based

https://doi.org/10.1038/s41560-023-01387-5

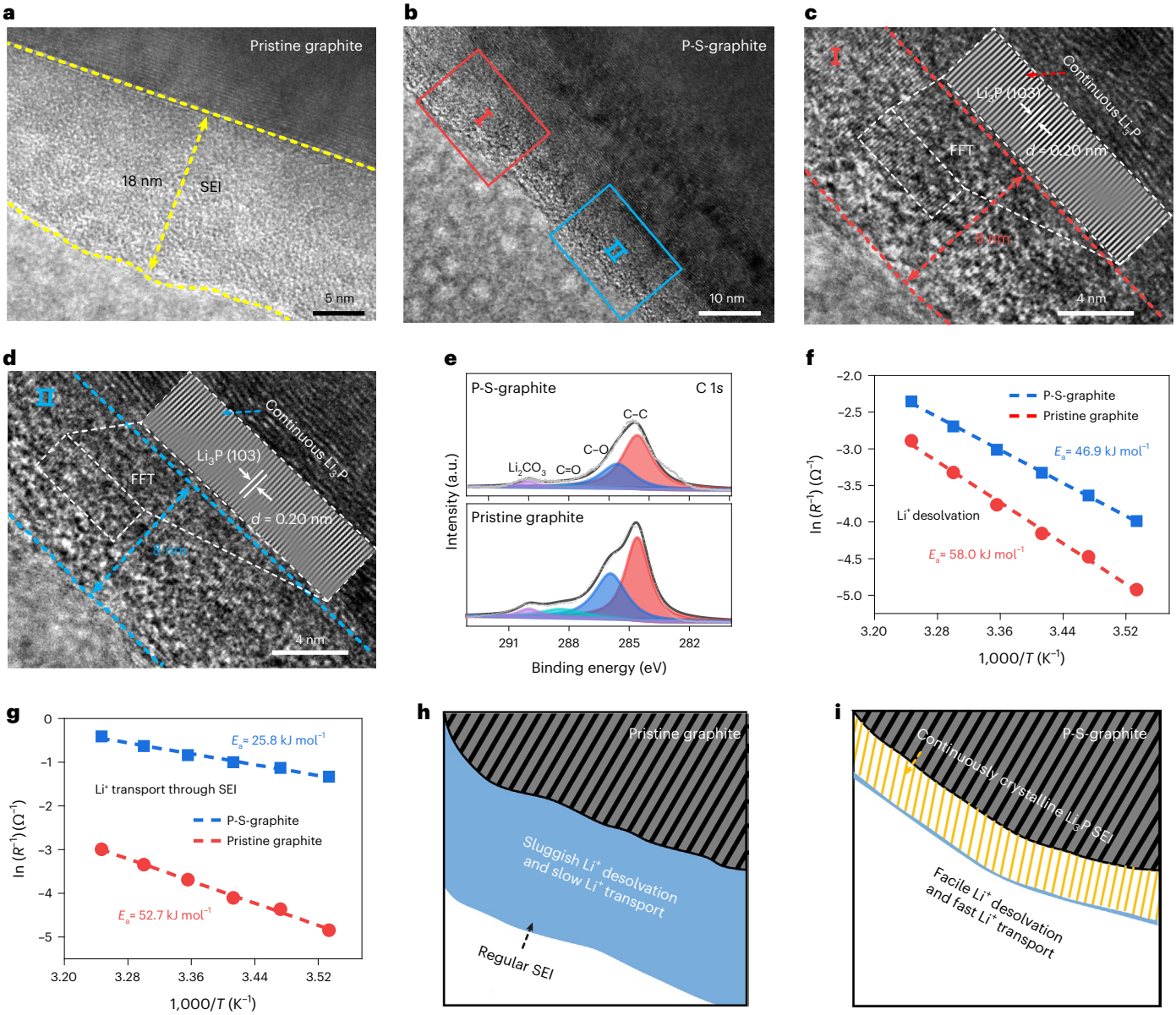

Fig. 3 | Characterization of Li_3P-based SEI on P-S-graphite. a,**b**, HRTEM images of cycled pristine graphite (**a**) and P-S-graphite (**b**). **c**,**d**, Magnified images of region I (**c**) and region II (**d**) as marked in **b**. **e**, High-resolution C 1*s* XPS spectra of cycled graphite anodes. **f**,**g**, Comparison of $E_{a,ct}$ (**f**) and $E_{a,SEI}$ (**g**) for the two graphite anodes. The activation energies were calculated by the classic Arrhenius law according to the EIS results. **h**,**i**, Schematics of interphases of pristine graphite (**h**) and P-S-graphite anodes (**i**). FFT, fast Fourier transform.

SEI of the P-S-graphite could simultaneously accelerate the Li^+ desolvation and Li^+ transport across the SEI (Fig. 3i), supporting its superior fast-charging capability.

Fast-charging capability with the Li_3P-based SEI

The fast-charging capability of the P-S-graphite anode was examined in pouch cells coupled with NCM622 cathodes over a voltage range of 2.9 to 4.25 V. As shown in Fig. 4a and Supplementary Fig. 24, the cells were tested using a practical constant current (CC)–constant voltage (CV) charging protocol with various CC charging rates ranging from 0.2 to 10C. The discharging current was fixed at 0.2C. 97.0%, 91.2%, 86.2% and 80.0% of the capacity (~2.3 mAh cm^{-2} for the anode with a negative/positive ratio of ~1.1) were achieved for the pouch cell using the P-S-graphite anode within 15, 10, 7.5 and 6 min (4C, 6C, 8C and 10C), respectively. In contrast, only 57.4% recharge was obtained for the pouch cell with the pristine graphite anode at 10C, and the cell showed a rapid capacity degradation during cycling.

Supplementary Fig. 25 and Fig. 4b present the charging/discharging profiles of pouch cells with different graphite anodes at various charging rates and the corresponding capacity contributions at the CC and CV charging states, respectively. The cells with P-S-graphite anodes delivered a much higher percentage of the capacity in the CC state compared with the cells with pristine graphite anodes. In particular, at the CC charging rate of 8C, the cells with P-S-graphite anodes achieved a high capacity contribution of 70% at the CC state, much higher than 25% for the cells with pristine graphite anodes. Compared with the P-S-graphite-based cells, the pristine graphite-based cells rapidly reached the cutoff voltage with large polarization (Supplementary Figs. 25 and 26), which was regarded as the major reason for metallic Li plating at the anode surface[38].

The state of charge versus time plots of cells also demonstrated the superior fast-charging capability of the P-S-graphite (Supplementary Fig. 27). Supplementary Table 2 and Fig. 4c compare the fast-charging capability of P-S-graphite with those reported in the literature, again

https://doi.org/10.1038/s41560-023-01387-5

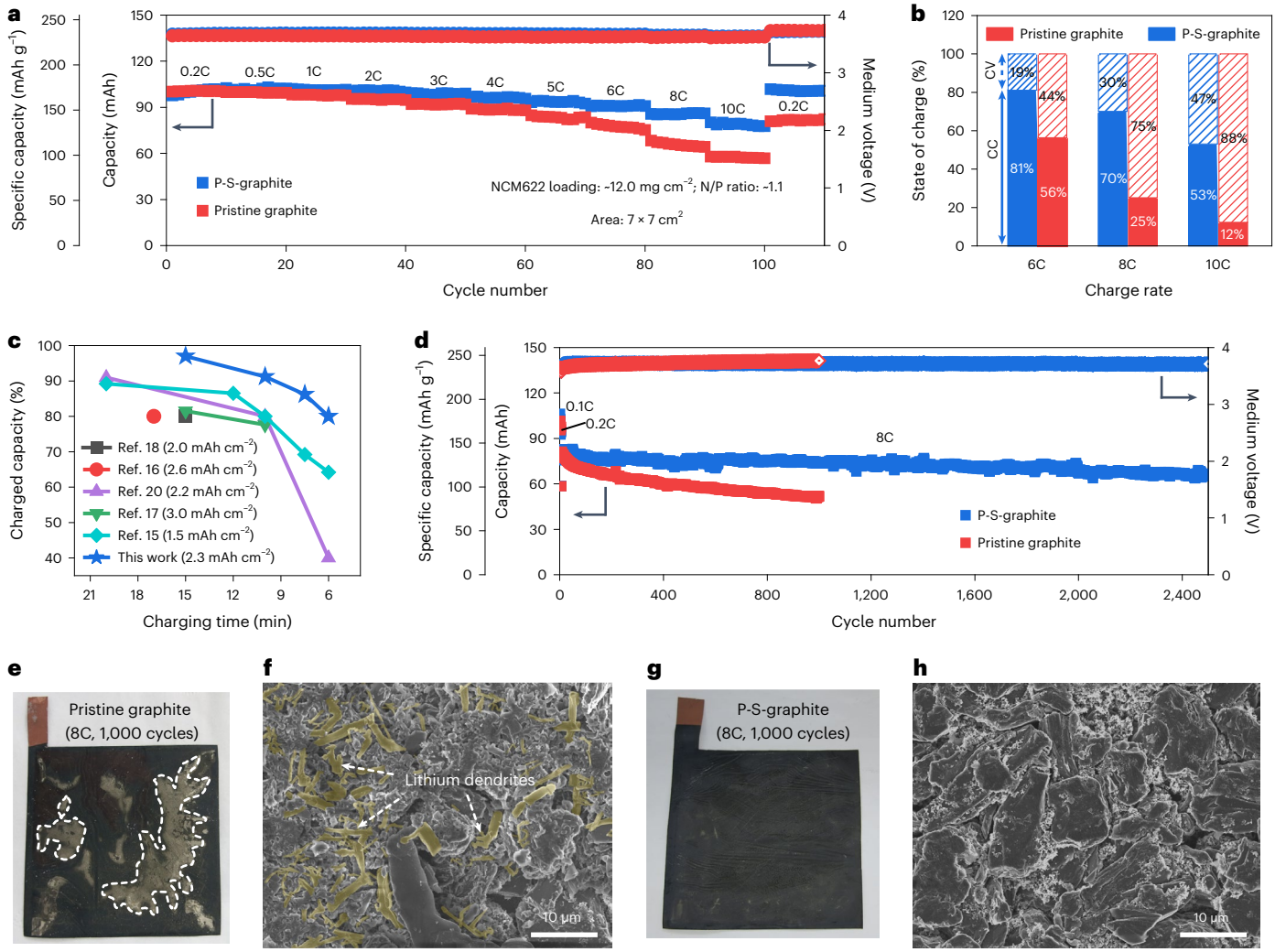

Fig. 4 | Electrochemical performance of graphite anode with Li_3P-based SEI. **a**, The fast-charging capability of the NCM622||graphite pouch cells with various charging currents ranging from 0.2C to 10C. **b**, Plots of the state of charge divided into CC/CV stages at each charging current density. **c**, Comparison of the fast-charging capability of P-S-graphite with the reported graphite anodes. **d**, Cycling performance of the NCM622||graphite pouch cells at a charging current of 8C. **e**,**f**, Optical photograph (**e**) and SEM image (**f**) of pristine graphite anodes after 1,000 cycles with a charging current of 8C. **g**,**h**, Optical photograph (**g**) and SEM image (**h**) of P-S-graphite anodes after 1,000 cycles with a charging current of 8C. N/P ratio, negative/positive ratio.

demonstrating the remarkable improvement in its fast-charging capability. Cycling stability under fast-charging conditions is an important parameter for practical implementation in fast-charging batteries. The cells with P-S-graphite anodes showed high capacity retentions of 81.7% (after 2,500 cycles) and 86.6% (after 1,500 cycles) at 8C and 6C (Fig. 4d and Supplementary Fig. 28), respectively, which was close to the cyclability of commercial batteries tested under low C rates. Thus, the attainment of the extremely fast-charging capability of cells with the P-S-graphite anodes did not sacrifice their cycling performance. In contrast, the cells with pristine graphite anodes displayed an increased overpotential during cycling (Supplementary Fig. 29) and showed a much lower capacity retention of 62.9% after 1,000 cycles at 8C (Fig. 4d).

We further investigated the morphology and microstructure of the two graphite anodes after 1,000 cycles at 8C. As shown by the digital and SEM images in Fig. 4e–h, abundant silvery grey deposits were observed on the cycled pristine graphite anode (Fig. 4e), which did not appear on the cycled P-S-graphite anode (Fig. 4g). Dendritic and mossy metallic Li structures were seen on these protrusions on the cycled pristine graphite anode under SEM (Fig. 4f). In contrast, a smooth, clean surface without Li deposits was observed on the P-S-graphite anode (Fig. 4h). The behaviour of metallic Li plating on a graphite anode would cause safety concerns and irreversible Li consumption during cycling. The latter would explain the capacity decay in the cells with the pristine graphite anodes under fast charging[9]. The capability of P-S-graphite to suppress the undesirable Li plating was further verified by in situ optical microscopy (Supplementary Fig. 30).

To further investigate the stability of the Li_3P-based SEI, the microstructure of the cycled P-S-graphite was characterized. The mapping images from energy dispersive X-ray spectroscopy verified that P was uniformly distributed on the surface of the cycled P-S-graphite (Supplementary Fig. 31), which was similar to the fresh counterpart. Transmission electron microscopy images showed a continuously crystalline Li_3P-based SEI with a thickness similar to that of the pristine structure for P-S-graphite after long-term fast-charging cycling (Supplementary Fig. 32). In addition, the resistance of the full cell with P-S-graphite remained stable during fast-charging cycling (Supplementary Fig. 33a). These results verify the good chemical and electrochemical stability of the Li_3P-based SEI, which effectively suppressed the continuous electrolyte decomposition and byproduct accumulation on the electrode surface during fast-charging cycling. In contrast, the thickness of the SEI on the pristine graphite and the resistance of the pristine graphite-based full cell increased with cycling due to the continuous

https://doi.org/10.1038/s41560-023-01387-5

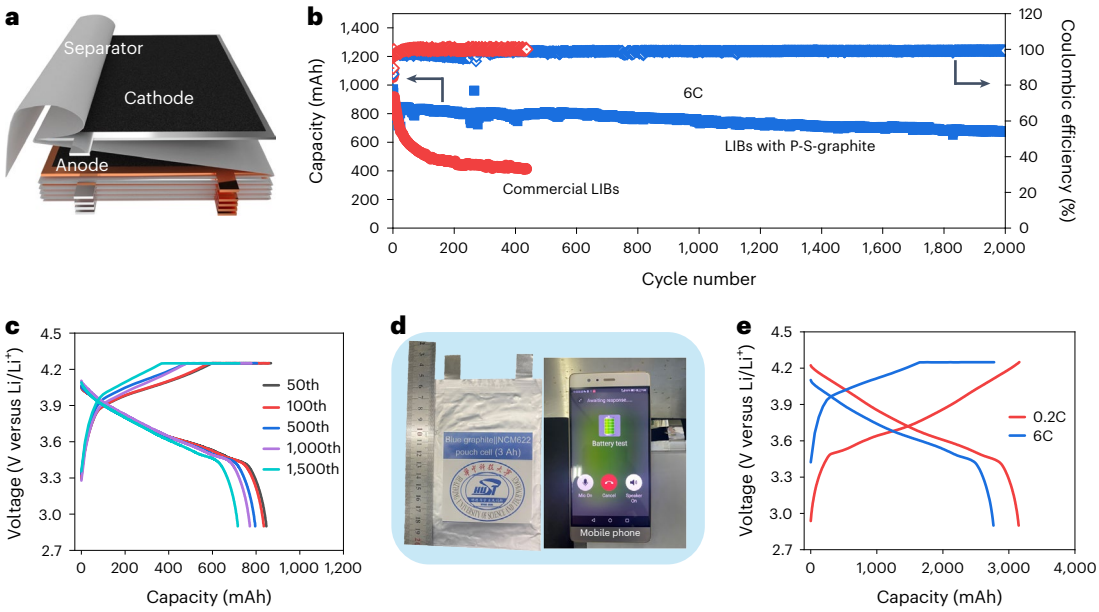

Fig. 5 | Fast-charging capability of a graphite anode with Li_3P-based SEI in Ah-level pouch cells. a, Schematic of a laminated pouch cell. **b**,**c**, Cycling performance of the laminated NCM622||graphite pouch cells (~1,000 mAh at 0.2C) (**b**) and the corresponding charging/discharging profiles for different cycles (**c**). **d**,**e**, Photographs (**d**) and charging/discharging profiles (**e**) of a laminated NCM622||P-S-graphite pouch cell (~3,100 mAh at 0.2C).

parasitic reaction between the active material and the electrolyte during cycling (Supplementary Figs. 33b and 34)[21,39].

To further demonstrate the potential of P-S-graphite for practical fast-charging LIBs, an Ah-level laminated pouch-type full cell consisting of a P-S-graphite anode and an NCM622 cathode was fabricated (Fig. 5a). The laminated NCM622||P-S-graphite pouch cell delivered a reversible capacity of 0.94 Ah at 0.2C and showed a high reversible capacity of 0.84 Ah at 6C. The cell sustained impressive cycling stability with 82.9% capacity retention for 2,000 cycles (Fig. 5b). The slight capacity decay could potentially be attributed to the degradation of the NCM622 cathode after long-term cycling under fast-charging conditions (Supplementary Fig. 35). The voltage-capacity profiles showed that only slight potential polarization occurred during long-term cycling (Fig. 5c). This superior fast-charging capability with a long lifespan has never been reported in an Ah-level laminated pouch cell, which highlighted the success of our continuously inorganic Li^+ conductive SEI design with reduced Li^+ desolvation energy in improving the reaction kinetics and cycling stability of the graphite anodes. In contrast, a counterpart with a pristine graphite anode displayed only 46% of the initial capacity after 400 cycles at 6C under the same test conditions (Fig. 5b). We further fabricated a 3.1 Ah-laminated pouch cell that successfully powered a mobile phone (Fig. 5d) after 10 min of recharge to 90.3% of the capacity. The detailed parameters of the cell are provided in Supplementary Table 3. After 10 min of charging, the energy density of this cell reached ~207.5 W h kg^{-1} (Fig. 5e), further demonstrating the practicability of the P-S-graphite anode for extremely fast-charging batteries. In consideration of the superior electrochemical performance, facile synthesis and low cost of the raw materials, P-S-graphite is potentially cost-effective and, thus, is promising for the battery industry.

Conclusions

In summary, we have systematically investigated the effect of various SEI components on the Li^+ solvation structure using MD and DFT calculations. We found that a low-solvent-coordination solvation structure can be formed near the IHP on the Li_3P species due to the strong interaction between Li^+ and Li_3P. This, together with the high ionic conductivity of Li_3P, contributes to the efficient Li^+ desolvation process and fast Li^+ migration across the SEI. Accordingly, we developed a P-S-graphite anode. A ~4.4-nm-thick, uniform S-bridged P layer was firmly bonded onto its surface, and continuously crystalline Li_3P-based SEI was produced in situ during cycling. As a result, an Ah-level pouch cell fabricated with the P-S-graphite anode and an NCM622 cathode displayed excellent fast-charging performance, stable cycling performance and high energy density under high-rate charging conditions. Our work highlights the importance of interfacial chemistry for the Li^+ solvation structure and SEI formation and could serve as a guide for the design of effective SEI components for fast-charging LIBs.

Methods

Preparation of P-S-graphite

Pristine graphite and a P/S hybrid with a mass ratio of 9:1 were placed and sealed in an Ar-filled reactor. The reaction system was heated from room temperature to 450 °C and held at this temperature for 3 h, and then it was cooled down to 280 °C and held for another 20 h. A uniform P layer finally formed on the graphite during the natural cooling process. The samples were collected after having cooled down to environmental temperature. To investigate the effect of S on the P deposition behaviour, P/S hybrids with different S/(S + P) mass ratios (0, 1/100, 2.5/100, 5/100 and 10/100) were used. With optimized S/(S + P) and (S + P)/graphite mass ratios (1/100, 3/100), P-S-graphite was achieved, featuring uniform surficial morphology and structure for electrochemical measurement. The primary role of S was to facilitate the formation of a uniform P coating on the graphite.

Material characterization

The morphology and structure of the samples were investigated with a Zeiss G300 SEM and an FEI Talos f200x TEM. X-ray diffraction was conducted using a PANalytical B.V. instrument with Cu $K\alpha_1$ radiation (λ = 0.154 nm, 40 kV, 40 mA). XPS analysis was performed using AXIS-ULTRA DLD-600W with Al Kα radiation. Raman spectra analysis was performed on LabRAM HR800, Horiba Jobin Yvon, equipped with a 532.4 nm laser. The elemental contents of samples were evaluated with an inductively coupled plasma (Agilent 7800).

Electrochemical tests

Graphite anodes were fabricated for electrochemical tests through a traditional slurry approach. The slurry consisted of 90 wt% active material, 5 wt% carbon black and 5 wt% polyacrylic acid. The mass loading and the tap density of the graphite anodes were ~7.0 mg cm^{-2} and ~1.4 g cm^{-3}, respectively. NCM622 cathodes with a mass loading of ~12.0 mg cm^{-2} were fabricated using a similar slurry approach. The slurry consisted of 92 wt% active material, 4 wt% carbon black and 4 wt% polyvinylidene fluoride. CR2032 coin cells and pouch cells were assembled in an argon-filled glovebox. Lithium foils were used in the half-cells as counter electrodes. The separator was Celgard 2500 polypropylene membrane, and the electrolyte was 1 M $LiFP_6$ in EC/DMC (v/v = 3:7). Graphite and NCM622 electrodes with a size of 7.8 × 8 cm^2 were used in the assembly of the laminated pouch cells. The electrolyte dosage for Ah-level pouch cells was ~3.8 g Ah^{-1} after the battery formation process. The charge/discharge measurements were recorded on a Neware battery test system (CT-4008T-5V-50mA-164, Shenzhen, China) and Land battery tester. CV and EIS measurements were conducted on an electrochemical workstation (Biologic VMP3). The CV was performed at a scan rate of 0.01 mV s^{-1} in a voltage window of 0.01–1.00 V. The EIS was conducted with a frequency range from 100 kHz to 10 mHz with an amplitude of 5 mV. To record the temperature-dependent EIS spectra, the cells were rested in different temperature conditions (10–35 °C) for ~20 min before measurement. The voltage range for the electrochemical performance measurement of full cells was 2.90–4.25 V. The charging protocol for full cells was optimized with the combination of constant current and constant voltage (CC–CV) charging. The current densities for CC charging varied from 0.2 to 10C. The corresponding total charging times (CC + CV) were fixed at 60, 20, 10, 7.5 and 6 min for 1C-CV, 3C-CV, 6C-CV, 8C-CV and 10C-CV, respectively. The discharging current for the full cells was fixed at 0.2C. To study the metallic lithium plating on the graphite anodes, full pouch cells were disassembled in an argon-filled glovebox after 1,000 cycles. The graphite anodes were then characterized.

Calculation methods

Classic MD simulations were performed using LAMMPS (ref. 40). The initial periodic systems were set up using PACKMOL (ref. 41) and Moltemplate (http://www.moltemplate.org/). The deposition of sulfur was simulated using the reaxFF potential[42]. The time steps for the MD were set to 1.0 and 0.25 fs for classic MD simulations and reaxFF simulations, respectively.

For the reaxFF simulations, NVT runs with heating from 298 to 600 K were performed for 75 ps to first heat the sulfur. Then, NVT runs at 600 K were performed for 125 ps to evaporate the sulfur. After the formation of sulfur vapour, the sulfur was deposited by cooling the temperature to 298 K for 75 ps and finally maintaining the temperature for 125 ps.

For the classic MD simulations of solvation structures near SEI, OPLS[43] force-field parameters combined with RESP charges[44,45] were utilized. The force-field parameters of various SEIs were taken from CVFF[46] and assigned with REPEAT[47] charges. The cutoff for the Lennard-Jones potential was set to 10 Å. The long-range Coulombic interactions were counted by a particle–particle particle-mesh[48]. The SEI was fixed during the simulations. First, Langevin dynamics were performed at 500 K for 0.5 ns to randomize the initial shape of the molecules. Then, we continued the simulation with NVT runs at 500 K for 1 ns to equilibrate the system. Next, a 3 ns NVT run was performed at 300 K. The solvation structures were obtained by statistically analysing the data from the last 2 ns of the trajectory. VESTA[49] and VMD[50] were employed to visualize the electrolyte structures. The potential of the mean force was extracted by using the metadynamics method, performed with the LAMMPS-COLVARS package[51].

The DFT calculations[52,53] were performed using Vienna Ab-initio Simulation Package[54] based on the projector augmented wave method[55]. A Perdew–Burke–Ernzerhof form[56,57] of the exchange-correlation functional was employed with van der Waals corrections (DFT-D3 method)[58]. The kinetic energy cutoff for the electronic wavefunction was set to 520 eV. The Brillouin zone sampling was performed using the Monkhorst–Pack scheme[59]. The adsorption energies (E_{ads}) were calculated as follows:

$$E_{ads} = E_{slab\text{-}ads} - E_{slab} - E_{ads} \quad (1)$$

where $E_{slab\text{-}ads}$ is the total energy for the absorbed surface of a species, E_{slab} is the energy of the SEI surface and E_{ads} is the energy of Li ions.

Data availability

All data are available in the article and its Supplementary Information files.

References

1. Liu, Y., Zhu, Y. & Cui, Y. Challenges and opportunities towards fast-charging battery materials. *Nat. Energy* **4**, 540–550 (2019).
2. Cai, W. et al. A review on energy chemistry of fast-charging anodes. *Chem. Soc. Rev.* **49**, 3806–3833 (2020).
3. Li, S. et al. Fast charging anode materials for lithium-ion batteries: current status and perspectives. *Adv. Funct. Mater.* **32**, 2200796 (2022).
4. Liu, H. et al. A disordered rock salt anode for fast-charging lithium-ion batteries. *Nature* **585**, 63–67 (2020).
5. Griffith, K. J., Wiaderek, K. M., Cibin, G., Marbella, L. E. & Grey, C. P. Niobium tungsten oxides for high-rate lithium-ion energy storage. *Nature* **559**, 556–563 (2018).
6. Meintz, A. et al. Enabling fast charging–vehicle considerations. *J. Power Sources* **367**, 216–227 (2017).
7. Ni, Q. et al. An extremely fast charging $Li_3V_2(PO_4)_3$ cathode at a 4.8 V cutoff voltage for Li-ion batteries. *ACS Energy Lett.* **5**, 1763–1770 (2020).
8. Tu, S. et al. Single-layer-particle electrode design for practical fast-charging lithium-ion batteries. *Adv. Mater.* **34**, 2202892 (2022).
9. Wang, C.-Y. et al. Fast charging of energy-dense lithium-ion batteries. *Nature* **611**, 485–490 (2022).
10. Lu, L. L. et al. Superior fast-charging lithium-ion batteries enabled by the high-speed solid-state lithium transport of an intermetallic Cu_6Sn_5 Network. *Adv. Mater.* **34**, 2202688 (2022).
11. Ahmed, S. et al. Enabling fast charging–a battery technology gap assessment. *J. Power Sources* **367**, 250–262 (2017).
12. Mao, C., Ruther, R. E., Li, J., Du, Z. & Belharouak, I. Identifying the limiting electrode in lithium ion batteries for extreme fast charging. *Electrochem. Commun.* **97**, 37–41 (2018).
13. Tian, R. et al. Quantifying the factors limiting rate performance in battery electrodes. *Nat. Commun.* **10**, 1933 (2019).
14. Jow, T. R., Delp, S. A., Allen, J. L., Jones, J.-P. & Smart, M. C. Factors limiting Li^+ charge transfer kinetics in Li-ion batteries. *J. Electrochem. Soc.* **165**, A361–A367 (2018).
15. Zhang, S. S., Ma, L., Allen, J. L. & Read, J. A. Stabilizing capacity retention of Li-ion battery in fast-charge by reducing particle size of graphite. *J. Electrochem. Soc.* **168**, 040519 (2021).
16. Baek, M., Kim, J., Jin, J. & Choi, J. W. Photochemically driven solid electrolyte interphase for extremely fast-charging lithium-ion batteries. *Nat. Commun.* **12**, 6807 (2021).
17. Chen, K. H. et al. Enabling 6C fast charging of Li-ion batteries with graphite/hard carbon hybrid anodes. *Adv. Energy Mater.* **11**, 2003336 (2020).
18. Sun, C. et al. 50C fast-charge Li-ion batteries using a graphite anode. *Adv. Mater.* **34**, 2206020 (2022).
19. Kazyak, E., Chen, K. H., Chen, Y., Cho, T. H. & Dasgupta, N. P. Enabling 4C fast charging of lithium-ion batteries by coating graphite with a solid-state electrolyte. *Adv. Energy Mater.* **12**, 2102618 (2021).

20. Lee, S. M. et al. A cooperative biphasic MoO_x-MoP_x promoter enables a fast-charging lithium-ion battery. *Nat. Commun.* **12**, 39 (2021).
21. Heiskanen, S. K., Kim, J. & Lucht, B. L. Generation and evolution of the solid electrolyte interphase of lithium-ion batteries. *Joule* **3**, 2322–2333 (2019).
22. Zhang, Z. et al. Capturing the swelling of solid-electrolyte interphase in lithium metal batteries. *Science* **375**, 66–70 (2022).
23. Chen, J. et al. Electrolyte design for LiF-rich solid–electrolyte interfaces to enable high-performance microsized alloy anodes for batteries. *Nat. Energy* **5**, 386–397 (2020).
24. Qin, N. et al. Over-potential tailored thin and dense lithium carbonate growth in solid electrolyte interphase for advanced lithium ion batteries. *Adv. Energy Mater.* **12**, 2103402 (2022).
25. Tan, J., Matz, J., Dong, P., Shen, J. & Ye, M. A growing appreciation for the role of LiF in the solid electrolyte interphase. *Adv. Energy Mater.* **11**, 2100046 (2021).
26. Jiang, L. L. et al. Inhibiting solvent co-intercalation in a graphite anode by a localized high-concentration electrolyte in fast-charging batteries. *Angew. Chem., Int. Ed.* **60**, 3402–3406 (2021).
27. Shi, J. et al. Improving the graphite/electrolyte interface in lithium-ion battery for fast charging and low temperature operation: fluorosulfonyl isocyanate as electrolyte additive. *J. Power Sources* **429**, 67–74 (2019).
28. Yang, Y. et al. Rechargeable $LiNi_{0.65}Co_{0.15}Mn_{0.2}O_2$||graphite batteries operating at −60 °C. *Angew. Chem., Int. Ed.* **61**, 202209619 (2022).
29. Yang, Y. et al. Synergy of weakly-solvated electrolyte and optimized interphase enables graphite anode charge at low temperature. *Angew. Chem., Int. Ed.* **61**, 202208345 (2022).
30. Sun, Y. et al. Design of red phosphorus nanostructured electrode for fast-charging lithium-ion batteries with high energy density. *Joule* **3**, 1080–1093 (2019).
31. Xu, K., von Cresce, A. & Lee, U. Differentiating contributions to 'ion transfer' barrier from interphasial resistance and Li^+ desolvation at electrolyte/graphite interface. *Langmuir* **26**, 11538–11543 (2010).
32. Li, Y. & Qi, Y. Energy landscape of the charge transfer reaction at the complex Li/SEI/electrolyte interface. *Energy Environ. Sci.* **12**, 1286–1295 (2019).
33. Xin, S. et al. Smaller sulfur molecules promise better lithium-sulfur batteries. *J. Am. Chem. Soc.* **134**, 18510–18513 (2012).
34. Zhou, J. et al. High-spin sulfur-mediated phosphorous activation enables safe and fast phosphorus anodes for sodium-ion batteries. *Chem* **6**, 221–233 (2020).
35. Chuang, C.-C., Hsieh, Y.-Y., Chang, W.-C. & Tuan, H.-Y. Phosphorus-sulfur/graphene composites as flexible lithium-sulfur battery cathodes with super high volumetric capacity. *Chem. Eng. J.* **387**, 123904 (2020).
36. Marino, C., El Kazzi, M., Berg, E. J., He, M. & Villevieille, C. Interface and safety properties of phosphorus-based negative electrodes in Li-ion batteries. *Chem. Mater.* **29**, 7151–7158 (2017).
37. Shi, P. et al. The synergetic effect of lithium bisoxalatodifluoro-phosphate and fluoroethylene carbonate on dendrite suppression for fast charging lithium metal batteries. *Small* **16**, 2001989 (2020).
38. Kim, N., Chae, S., Ma, J., Ko, M. & Cho, J. Fast-charging high-energy lithium-ion batteries via implantation of amorphous silicon nanolayer in edge-plane activated graphite anodes. *Nat. Commun.* **8**, 812 (2017).
39. Huang, W. et al. Evolution of the solid-electrolyte interphase on carbonaceous anodes visualized by atomic-resolution cryogenic electron microscopy. *Nano Lett.* **19**, 5140–5148 (2019).
40. Plimpton, S. Fast parallel algorithms for short-range molecular dynamics. *J. Comput. Phys.* **117**, 1–19 (1995).
41. Martínez, L., Andrade, R., Birgin, E. G. & Martínez, J. M. PACKMOL: a package for building initial configurations for molecular dynamics simulations. *J. Comput. Chem.* **30**, 2157–2164 (2009).
42. Monti, S., Carravetta, V. & Ågren, H. Simulation of gold functionalization with cysteine by reactive molecular dynamics. *J. Phys. Chem. Lett.* **7**, 272–276 (2016).
43. Jorgensen, W. L., Maxwell, D. S. & Tirado-Rives, J. Development and testing of the OPLS all-atom force field on conformational energetics and properties of organic liquids. *J. Am. Chem. Soc.* **118**, 11225–11236 (1996).
44. Bayly, C. I., Cieplak, P., Cornell, W. & Kollman, P. A. A well-behaved electrostatic potential based method using charge restraints for deriving atomic charges: the RESP model. *J. Phys. Chem.* **97**, 10269–10280 (1993).
45. Lu, T. & Chen, F. Multiwfn: a multifunctional wavefunction analyzer. *J. Comput. Chem.* **33**, 580–592 (2012).
46. Dauber-Osguthorpe, P. et al. Structure and energetics of ligand binding to proteins: *Escherichia coli* dihydrofolate reductase-trimethoprim, a drug-receptor system. *Proteins: Struct. Funct. Bioinforma.* **4**, 31–47 (1988).
47. Campañá, C., Mussard, B. & Woo, T. K. Electrostatic potential derived atomic charges for periodic systems using a modified error functional. *J. Chem. Theory Comput.* **5**, 2866–2878 (2009).
48. Hockney, R. W. & Eastwood, J. W. *Computer Simulation Using Particles* (CRC Press, 2021).
49. Momma, K. & Izumi, F. VESTA 3 for three-dimensional visualization of crystal, volumetric and morphology data. *J. Appl. Crystallogr.* **44**, 1272–1276 (2011).
50. Humphrey, W., Dalke, A. & Schulten, K. VMD: visual molecular dynamics. *J. Mol. Graph.* **14**, 33–38 (1996).
51. Fiorin, G., Klein, M. & Hénin, J. Using collective variables to drive molecular dynamics simulations. *Mol. Phys.* **111**, 3345–3362 (2013).
52. Hohenberg, P. & Kohn, W. Inhomogeneous electron gas. *Phys. Rev.* **136**, B864 (1964).
53. Kohn, W. & Sham, L. J. Self-consistent equations including exchange and correlation effects. *Phys. Rev.* **140**, A1133 (1965).
54. Kresse, G. & Hafner, J. Ab initio molecular dynamics for liquid metals. *Phys. Rev. B* **47**, 558 (1993).
55. Blöchl, P. E. Projector augmented-wave method. *Phys. Rev. B* **50**, 17953 (1994).
56. Kresse, G. & Furthmüller, J. Efficient iterative schemes for ab initio total-energy calculations using a plane-wave basis set. *Phys. Rev. B* **54**, 11169 (1996).
57. Perdew, J. P., Burke, K. & Ernzerhof, M. Generalized gradient approximation made simple. *Phys. Rev. Lett.* **77**, 3865 (1996).
58. Grimme, S., Antony, J., Ehrlich, S. & Krieg, H. A consistent and accurate ab initio parametrization of density functional dispersion correction (DFT-D) for the 94 elements H–Pu. *J. Chem. Phys.* **132**, 154104 (2010).
59. Monkhorst, H. J. & Pack, J. D. Special points for Brillouin-zone integrations. *Phys. Rev. B* **13**, 5188 (1976).

Acknowledgements

This work is financially supported by the Natural Science Foundation of China (Grant No. 52072137). We would like to thank the Analytical and Testing Center of Huazhong University of Science and Technology for providing the facilities to conduct the transmission electron microscopy characterizations.

Author contributions

Y.S. and S.T. conceived the idea for this work. S.T. performed the material characterizations and electrochemical measurements with assistance from Y.Z., Z.C., X.W., R.Z., Y.O., W.W., X.L. and X.D. B.Z. performed the MD simulations and DFT calculations. L.W. discussed

and edited the results. S.T. and B.Z. co-wrote the original paper. Y.S. reviewed and edited the paper.

Competing interests
The authors declare no competing interests.

Additional information
Supplementary information The online version contains supplementary material available at https://doi.org/10.1038/s41560-023-01387-5.

Correspondence and requests for materials should be addressed to Yongming Sun.

Peer review information *Nature Energy* thanks James Tour and the other, anonymous, reviewer(s) for their contribution to the peer review of this work.

Reprints and permissions information is available at www.nature.com/reprints.

Publisher's note Springer Nature remains neutral with regard to jurisdictional claims in published maps and institutional affiliations.